



In-flight receiver calibration of the Ganymede Laser Altimeter (GALA) by passive Earth observations

Gaku Nishiyama^{1,2}, Alexander Stark¹, Klaus-Dieter Matz¹, Christian Hüttig¹, Kai Wickhusen¹,
 Livio Agostini³, Christian Althaus¹, Jan Binger¹, Keigo Enya^{4,5}, Janot George¹, Kay Lingenauber¹,
 Jun Kimura⁶, Masanori Kobayashi⁷, Giulio Macrì^{8,1}, Wladimir Neumann^{1,9}, Luca Penasa¹⁰,
 Ganna Portyankina¹, Cecilia Tubiana³, Konrad Wilner¹, Pasquale Palumbo³, and Hauke Hussmann¹

¹Institute of Space Research, German Aerospace Center (DLR), Rutherfordstraße 2, 12489, Berlin, Germany

²Department of Earth and Planetary Science, The University of Tokyo, 7-3-1 Hongo, Bunkyo-ku, Tokyo, 113-0033, Japan

³INAF-IAPS (Istituto di Astrofisica e Planetologia Spaziali), Via Fosso del Cavaliere 100, 00133, Rome, Italy

⁴Institute of Space and Astronautical Science, Japan Aerospace Exploration Agency, 3-1-1 Yoshinodai, Chuo-ku, Sagamihara, Kanagawa 252-5210, Japan

⁵The Graduate University for Advanced Studies, SOKENDAI, Hayama, Miura-gun, Kanagawa 240-0193, Japan

⁶Department of Earth and Space Science, The University of Osaka, 1-1 Machikaneyama-cho, Toyonaka, Osaka 560-0043, Japan

⁷Planetary Exploration Research Center, Chiba Institute of Technology, 2-17-1 Tsudanuma, Narashino, Chiba 275-0016, Japan

⁸Dipartimento di Fisica e Astronomia “Galileo Galilei”, Università di Padova, Vicolo dell’Osservatorio 3, 35122 Padova, Italy

⁹Institute of Geodesy and Geoinformation Science, Technische Universität Berlin, Kaiserin-Augusta-Allee 104-106, 10553 Berlin, Germany

¹⁰INAF-OAPd (Osservatorio Astronomico di Padova), Vicolo Osservatorio 5, 35122, Padova, Italy

Correspondence: Gaku Nishiyama (gaku.nishiyama@dlr.de)

Abstract. Post-launch characterization of the receiver telescope of the laser altimeter is essential for achieving precise georeferenced planetary measurements and for radiometric calibration to passively measure surface reflectance. For the Ganymede Laser Altimeter (GALA) aboard the Jupiter Icy Moons Explorer (Juice), such in-flight calibration was originally planned during a lunar flyby but could not be performed due to an unexpected reboot of the instrument. Instead, this study reports a passive noise measurement acquired during the Earth-farewell campaign on 9 September 2024 as an alternative opportunity for in-flight calibration. Using temporal variations in the GALA noise level as a proxy for photon flux incident on the GALA detector, we combine a theoretical noise model with Earth images obtained by the Jovis Amorum ac Natorum Undique Scrutator (JANUS) imager to constrain the GALA receiver boresight direction. By comparing the timing, magnitude, and temporal pattern of noise variations between observations and simulations, we find that the pre-launch boresight vector is inconsistent with the Earth-farewell observations. Our results further suggest that the GALA receiver boresight may have experienced a post-launch offset over $700 \mu\text{rad}$, although a definitive conclusion can be drawn only with additional cruise-phase data. The methodology developed in this study offers a framework for in-flight alignment calibration of GALA during future flybys, which is also broadly applicable to other planetary laser altimeters. The radiometric calibration performed in study is also prerequisite for the interpretation of passive albedo measurements of Jupiter and the Galilean moons.



15 1 Introduction

Laser altimeters have been one of the most commonly-installed instruments on lunar and planetary exploration missions. The basic functionality of onboard laser altimeters is to measure the range between a spacecraft and planetary surface based on the travel time of laser pulses. Range data acquired by laser altimeters are used to derive surface topography (e.g., Araki et al., 2009; Smith et al., 2017), as well as tidal deformations and rotation states (e.g., Stark et al., 2015a, b; Xiao et al., 2025) to gain 20 insights into planetary interior structure. Also, lateral variations in surface roughness, slope, and albedo can be characterized to investigate surface geologic processes (e.g., Neumann et al., 2003; Smith et al., 2017; Deutsch et al., 2024; Nishiyama et al., 2022, Nishiyama et al. under review in PSJ). Laser altimeters also play an important role in spacecraft navigation during landing operations (e.g., Kikuchi et al., 2021; Mizuno et al., 2017; Daly et al., 2017).

To achieve these scientific objectives and operations, precise determination of the laser altimeter alignment with respect to 25 spacecraft reference system is essential for the accurate estimation of footprint positions on the surface of a celestial body. Alignment information is typically determined during pre-launch phase after integration of the laser altimeter into the spacecraft. However, launch-induced vibration and/or difference in thermal conditions in space may cause deviations from the pre-launch alignment. Therefore, post-launch in-flight calibration of the laser altimeter needs to be performed using several 30 methods. For example, direct two-way laser ranging between a spacecraft and satellite laser ranging stations on the Earth can be used to characterize laser alignment as well as laser beam patterns (e.g., Smith et al., 2006, 2017; Barker et al., 2018; Noda et al., 2017, 2023). In addition, comparisons between laser altimeter profiles and images and/or image-based topography can be used to determine the alignment of laser altimeters (e.g., Noda et al., 2021).

Such a post-launch calibration has not yet been conducted for the Ganymede Laser altimeter (GALA)(Hussmann et al., 2025) onboard the Jupiter Icy Moons Explorer (Juice) mission. Similar to previous laser altimeters on planetary exploration 35 missions, GALA aims to provide surface topography data of icy moons, enabling investigations of geologic processes such as ice tectonics, cryovolcanism and impact cratering. Moreover, GALA targets measurements of Ganymede's tidal deformation induced by Jupiter to gain insights into its interior structure and the possible presence of a subsurface ocean (e.g., Kamata et al., 2016; Kimura et al., 2019; Hussmann et al., 2019; Enya et al., 2022). In order to accomplish these measurements with accurate 40 georeferencing, the boresight direction of GALA needs to be characterized after the launch of the Juice spacecraft in April 2023. As the Juice spacecraft is equipped with the Jovis Amorum ac Natorum Undique Scrutator (JANUS) imager (Palumbo et al., 2025), precise co-registration of GALA's boresight vector with JANUS images allows us to improve interpretation of the altimeter data in combination with surface imagery.

Determination of GALA's boresight vector in conjunction with JANUS images was originally planned to be performed 45 during the lunar flyby of the Lunar Earth Gravity Assist (LEGA) maneuver, which took place from 19 to 20 August 2024 (Stark et al., 2024). GALA was planned to be switched on prior to the Juice's closest approach to the Moon and to acquire topographic profiles of the lunar surface as its first in-cruise opportunity. In addition, JANUS was expected to potentially detect GALA's laser pulses reflected from the lunar surface by taking long exposures for lunar nightside images, enabling more accurate geometric calibration. However, the goal was not achieved during this calibration opportunity. Although JANUS



was operated successfully during the lunar flyby, GALA failed to fire laser pulses while pointing toward the Moon due to an
50 unexpected reboot of the instrument.

Instead, GALA had another opportunity for in-flight calibration during the Earth-farewell campaign on 9 September 2025. In this campaign, Juice observed the Earth from a distance of 5.65 million kilometers. Although the Earth was too far away for GALA to detect return pulses, GALA was operated in a passive mode. In this mode, GALA functioned as a single-pixel telescope and recorded a temporal variation in its noise level (Fig. 1a). Because the noise level is dependent on the amount of
55 light reaching the avalanche photodiode (APD) used in the GALA detector, variations in the GALA noise level are indicative of changes in brightness within its field of view (FOV). This noise variation, in turn, corresponds to temporal variations in the spacecraft attitude with respect to the Earth. Simultaneously, JANUS obtained images of the Earth using all of its filters, enabling a direct comparison between the GALA noise data and the spatial distribution of reflected sunlight on the Earth. Thanks to the accurate alignment between JANUS and the spacecraft reference frame, through star fields imaging, the boresight
60 vector of the GALA telescope with respect to spacecraft can be accurately determined through the JANUS-GALA comparison. While this comparison cannot derive the transmission direction of laser pulses, the line of sight of GALA's receiver (denoted as Rx-LoS hereafter) may be inferred to provide insights into the GALA alignment condition.

In this paper, we demonstrate boresight vector calibration using the GALA noise data obtained during the Earth-farewell campaign. Based on a theoretical prediction of the dependence of the GALA noise level on incoming solar flux, we establish
65 a method to directly compare the GALA noise level with the JANUS images taken at the same time. Using this method, we report the implications of the Earth-farewell campaign for the GALA alignment and discuss prospects for future GALA measurements.

2 Data

2.1 GALA

70 During the Earth-farewell campaign, GALA was operated in a passive mode for a total of 55 minutes, for which GALA was capable of detecting variations in incoming light at the 1064-nm wavelength as fluctuations of the noise level. Due to the discrete nature of photon arrivals and the subsequent stochastic processes of electron-hole pair generation within the APD, photons incident on GALA introduce additional noise atop of other noise sources, such as dark current. This additional noise is called solar noise. The magnitude of solar noise is proportional to the square root of the incident photon flux and can dominate
75 the overall noise level of GALA when its telescope is pointed toward a sufficiently bright body (see details in Sect. 3.2).

The noise level of GALA was observed as the root-mean-square (RMS) of the electrical signals within every range window. When GALA finds return pulses from electrical signals with a digital matching method (Hussmann et al., 2025), the receiver chain samples the electrical signal at intervals of 5 ns by combining two Analog-to-Digital Converters (ADCs). All electrical signals within the full range window of 40.48 μ s are recorded as range window samples composed of 8192 points in total.
80 Although the full range window sample data were transmitted to the Earth only at intervals of 3 seconds, the RMS of the



range window samples was computed onboard and transmitted to the Earth with a observation frequency of 30.3 Hz, enabling characterization of the the noise level for all observation cycles.

The noise data acquired during the Earth-farewell campaign clearly exhibit solar noise generated by sunlight reflected from Earth, as seen in Figure 1a. After the warm-up phase of the instrument, characterized as relatively high noise level at the beginning, the noise RMS stays at approximately 1.12 mV. Around 09:38:38 (UTC), the noise level began to increase and remained elevated at 3.0–3.5 mV until it returned back to its original level around 10:08:07 (UTC). This period of increased noise roughly coincides with the duration when GALA's FOV was pointed toward the Earth. Figure 1b shows the angular separation between the centers of the Earth and GALA Rx-LoS. When the angular separation is smaller than the Earth's apparent radius, the observed noise was at the increased level, implying contribution from the solar noise. Notably, the noise RMS also exhibits significant fluctuations while the GALA FOV was pointed at the Earth, reflecting temporal variations in photon flux collected by the GALA telescope.

For the latter analysis, we use the RMS of GALA noise data after smoothing out statistical variation. Due to the limited number of data points in every range window, the RMS values computed onboard are subject to statistical uncertainty, as seen in Fig. 1a. Therefore, the RMS noise were smoothed out using a moving average with a 0.5-seconds window to enable comparison with the temporal variation of the incoming photon flux (the black line in Fig. 1a).

2.2 JANUS

To compare the temporal variation of the GALA noise level, we use radiance variations based on JANUS observations with filter-12. JANUS is equipped with 13 filters, including 12 narrowband filters and one broadband filter, covering a spectral range from 0.34 to 1.08 μm (Palumbo et al., 2025). These filters enable measurements of spectral characteristics of the surface and atmosphere of Jupiter and its icy moons (e.g., Tosi et al., 2024; Fletcher et al., 2023). For comparison with the GALA data obtained at 1064-nm wavelength, images acquired with filter-12 are suitable. The wavelength coverage of filter-12 spans from 949 to 1081 nm, covering the wavelength of GALA (see more details in Sect. 3.1).

During the Earth-farewell campaign, JANUS obtained images using all filters while the GALA FOV overlapped with the Earth (Fig. 1a and b). In total, 168 images of the Earth were obtained. In this study, we use a filter-12 image taken at 09:57:02 (Fig. 1c) because this image has the highest quality without saturation. This approach implicitly assumes that the spatial radiance pattern of the Earth remains constant while the GALA FOV overlaps with the Earth. This assumption introduces only minor errors in the latter analysis because the time offset between the JANUS image acquisition and GALA noise increase is less than 20 minutes. On the Earth, cloud motion within 20 minutes is smaller than the pixel size of JANUS, which was 42 km at the Earth-Juice distance during this campaign. The Earth's rotation within 20 minutes corresponds to a longitudinal shift of at most 5 degree; this effect is explicitly accounted for in the latter analysis by calculating the corresponding latitudes and longitudes of each pixel on the Earth.



2.3 Attitude of Juice spacecraft

Another important factor is the temporal resolution of the spacecraft attitude information. The pointing direction of the GALA FOV can be computed from the spacecraft attitude information using the Spacecraft, Planet, Instrument, C-matrix, Events 115 (SPICE) Toolkit (Acton et al., 2018; Annex et al., 2020). To correlate the GALA noise data with temporal variation of pointing direction with respect to the Earth, Juice attitude information sampled at intervals comparable to the timescale of GALA noise variation is required. However, during the Earth-farewell campaign, the Juice attitude data were acquired only at one-minute intervals, making it difficult to use the Juice attitude information directly in the analysis.

To compensate for the limited temporal resolution of the Juice attitude data, we interpolated the spacecraft attitude by 120 employing three interpolation methods: linear interpolation, Piecewise Cubic Hermite Interpolating Polynomial (PCHIP) interpolation (Fritsch and Butland, 1984), and Akima interpolation (Akima, 1970). Both PCHIP and Akima methods fit piecewise cubic polynomials with different constraints: PCHIP preserves monotonicity while maintaining continuity of the first derivative, whereas Akima interpolation estimates derivatives locally using a weighted average of slopes from neighboring samples (see Fritsch and Butland (1984) and Akima (1970) for details). By applying these interpolations to the quaternions that define 125 the rotation matrix of the spacecraft attitude in the J2000 frame, we modeled high-resolution Juice attitude data. Note that other spline interpolation methods were found to be unsuitable, as they introduced overshooting between the coarsely sampled attitude points, resulting in unrealistic variations in the GALA pointing direction.

3 Method

A direct comparison between GALA and JANUS data is not straightforward because of differences in both wavelength coverage and observation data type. First, GALA detects photons within a narrow wavelength range of approximately 3-nm around 130 1064 nm, while filter-12 of JANUS collects photons over a broader spectral range. Second, the GALA observation in the passive mode consists of electrical noise signals whose amplitude needs to be quantitatively related to the photon flux incident on the APD. In this study, we convert radiance observed by JANUS into photon flux reaching the GALA APD by considering differences in spectral sensitivity between GALA and JANUS. We then apply a theoretical relationship between solar noise 135 and the incoming photon flux to compare the observed and predicted noise levels.

3.1 Conversion from JANUS radiance data to photon flux incident on GALA APD

Accounting for the difference in spectral sensitivity is essential for cross-calibration between measurements acquired by different instruments, as demonstrated in numerous previous studies (e.g., Pieters et al., 2013; Besse et al., 2013; Ohtake et al., 2013; Yumoto et al., 2024; Nishiyama et al., 2025). In this study, by incorporating the transmittance of the GALA bandpass 140 filter, we compute the ratio of radiance collected by GALA to that measured by JANUS as

$$r_{G/J} = \frac{\int R_G d\lambda}{\int R_J d\lambda} = 0.0326, \quad (1)$$



where R_G is the transmittance of the GALA bandpass filter from Enya et al. (2022), and R_J is the wavelength coverage of JANUS's filter-12 from Palumbo et al. (2025). Because the JANUS image used in this study is calibrated as total radiance integrated over the filter coverage, R_J is approximated as a uniform rectangular response spanning wavelengths from 949 to

145 1081 nm.

Using this conversion ratio, the optical power of the photon flux reaching the GALA APD is calculated as

$$P_G = \epsilon_t \epsilon_o r_{G/J} E_J A_{FOV} \Omega_{FOV}, \quad (2)$$

where ϵ_t is the optical transmission efficiency of the GALA telescope, ϵ_o is the optical efficiency of the GALA back-end optics, E_J is the radiance measured by JANUS and averaged over the GALA FOV, A_{FOV} is the area of the GALA FOV at 150 the Earth-Juice distance, and Ω_{FOV} is the solid angle of GALA's telescope aperture seen from the Earth. Due to degradation possibly caused by contamination and/or particles, ϵ_t and ϵ_o are expected to potentially decrease from 0.95 to 0.83 and from 0.875 to 0.8, respectively, over the entire mission (Hussmann et al., 2025). As GALA components are expected to experience minimal degradation shortly after the launch, we adopt the upper-end values for both ϵ_t and ϵ_o .

A_{FOV} and Ω_{FOV} are expressed as

$$155 \quad A_{FOV} = \pi \theta_{FOV}^2 D_{Earth}^2, \quad (3)$$

$$\Omega_{FOV} = \pi \left[\arctan \left(\frac{r_{FOV}}{D_{Earth}} \right) \right]^2, \quad (4)$$

where θ_{FOV} is the angular radius of the telescope FOV, D_{Earth} is the distance between the Earth and Juice spacecraft, and r_{FOV} is the telescope radius. All parameters used in the calculation are summarized in Table 1.

Table 1. Parameters used in the calculation of GALA noise.

Parameter	Symbol	Value	Unit
Optical transmittance of telescope	ϵ_t	0.95	–
Optical efficiency of back-end optics	ϵ_o	0.875	–
APD quantum efficiency	ϵ_q	0.41	–
GALA wavelength	λ_G	1064	nm
Amplification gain	G_{amp}	5.45	–
APD multiplication gain	M	94.9	–
Noise excess factor	x	0.25	–
APD bandwidth	B_0	100	MHz
APD transimpedance	R_i	33	kΩ
Telescope FOV radius	θ_{FOV}	225	μrad
Telescope radius	r_{FOV}	12.5	cm
Earth-Juice distance	D_{Earth}	5.65	Million km



It should be noted that this calculation implicitly assumes a flat spectral radiance over the wavelength coverage of the JANUS filter-12. However, artifacts due to different shape of the spectral radiance of the Earth are expected to be limited. For example, when non-flat spectra representative of continent, seawater, and clouds on the Earth based on calculation with Planetary Spectral Generator (PSG; Villanueva et al., 2018) are incorporated, $r_{G/J}$ results in 0.0306, 0.0332, 0.0290, respectively. Note that the PSG calculation assumed spectral properties of continent, seawater, and clouds based on spectral catalogs from Madden and Kaltenegger (2018), Clark et al. (2007), and Bohren and Huffman (1998), respectively. Thus, potential systematic errors due to spectral shape difference is limited to 9 % at most. This level of uncertainty is sufficiently small compared to variations in absolute reflectance among different area types of the Earth; for instance, the cloud reflectance can be an order of magnitude larger than that of seawater. Therefore, we adopt $r_{G/J}$ of 0.0326 based on the flat-spectrum assumption uniformly in the latter analysis.

3.2 Theoretical relationship between incoming photon flux and GALA noise

In general, the noise level of a laser altimeter in a passive mode can be expressed as (e.g, Steinbrügge et al., 2018)

$$N_{total} = \sqrt{N_{ds}^2 + N_{db}^2 + N_{sn}^2}, \quad (5)$$

where N_{ds} is the APD surface dark current noise, N_{db} is the APD bulk dark current noise and N_{sn} is the noise component induced by reflected sunlight incident on the APD. Note that the shot noise and electromagnetic compatibility noise are omitted from Equation 5 because GALA does not fire any laser pulses in the passive observation.

Since N_{ds} and N_{db} are constant, (i.e., independent of the incident photon flux), the background noise level of 1.12 mV observed before and after the Earth overlap corresponds to $\sqrt{N_{ds}^2 + N_{db}^2}$. The other component of noise, N_{sn} , is expressed as

$$I_{sn} = \frac{q\epsilon_q P_G \lambda_G}{hc}, \quad (6)$$

$$N_{sn} = G_{amp} \sqrt{2qI_{sn} M^{2+x} B_0 R_i^2}, \quad (7)$$

where q is the elemental charge, ϵ_q is the APD quantum efficiency, λ_G is the GALA wavelength, h is the Plank constant, c is the speed of light, G_{amp} is the GALA receiver amplification gain, M is the APD multiplication gain, x is the noise excess factor, B_0 is the APD band width, and R_i is the APD transimpedance. All values used in our calculation are summarized in Table 1.

4 Results

Comparison between the observation and simulations can be performed using two observables. First, the timings at which the observed noise level began to increase and subsequently returned to the background level may be used, as these transitions are clear indicators of onset and termination of the Earth-FOV overlap. Second, the absolute magnitude and temporal variation of the GALA noise can be used for a direct quantitative comparisons between the observation and simulations. Since the noise increase induced by photon flux reaching the GALA APD can be computed using the formulations in Sect. 3, the magnitude



and variability of the reflected sunlight can be directly compared with the observed noise data by taking the JANUS-based
190 radiance averaged within the GALA FOV as a function of time. In this section, we present comparisons between simulations
and observations from both perspectives.

4.1 Start and end of the noise increase

Figure 2 presents the observed noise RMS zoomed in around the onset and termination of the noise increase, along with
schematic illustrations of the relative position of the GALA FOV with respect to the Earth at those times. Since the duration of
195 the noise increase corresponds to period during which the GALA FOV overlaps with the Earth, the onset of the rapid rise in the
RMS value (red arrow in Fig. 2a) indicates the moment when the Earth started to enter the GALA FOV. Conversely, the time
at which the noise RMS dropped to the background level (red arrow in Fig. 2b) indicates when the Earth completely exited the
GALA FOV.

The observed timings of the onset and termination of the noise increase do not agree with simulations assuming that the pre-
200 launch boresight vector of the GALA Rx-LoS remains unchanged during cruise. Figure 2 also shows the simulated start and
end timings of the noise increase based on the SPICE-based simulations of the GALA FOV intersecting the Earth. Although
the simulated timings depend on the different interpolation methods used to increase the temporal resolution of the Juice
attitude information, none of the simulated results are consistent with the observations. At the start of the overlap, the linear
interpolation predicts a later onset of the overlap, whereas the PCHIP and Akima interpolation predict earlier onsets. At the
205 end of the overlap, all the interpolation methods predict an earlier decrease of the noise level, with discrepancies exceeding 13
seconds. These results suggest that the observations cannot be reproduced with the pre-launch boresight vector.

It should be noted that such timing discrepancies cannot be explained by the Earth's atmosphere. For example, images taken
by Earth-observing satellites like Himawari-8/9 (e.g., Okuyama et al., 2018) show a bright atmospheric halo of the Earth with
a thickness of approximately 30 km. However, its effect on the overlap timings is less than 0.3 seconds (colored bands in Fig.
210 2) and is negligible compared to the discrepancies between the observation and simulations.

A possible reason that may explain the timing gaps is an offset of the boresight vector of the GALA Rx-LoS after the launch,
as any deviation from the true boresight vector introduces systematic differences between the simulated and observed overlap
timings. To investigate such a post-launch offset, we repeated the comparisons shown in Fig. 2, changing the assumed GALA
boresight vector of the GALA FOV. For each assumed boresight direction, the start and end times of the noise increase were
215 simulated using different interpolation methods of the Juice attitude and compared with the observations.

Figure 3 shows maps of the timing discrepancies as a function of the assumed boresight vector direction in the spacecraft
reference frame. For the start of the overlap, the boresight vectors consistent with the observation differ among the assumed
interpolation methods. The linear interpolation yields a crescent-shaped region located to the right of the pre-launch boresight
vector, whereas the corresponding regions obtained with PCHIP and Akima interpolations are located rather to the left of the
220 pre-launch value (Fig. 3a, d, and g). Note that the crescent shape reflects the shape of the Earth's limb. In contrast, for the end
of the overlap, the crescent-shaped parameter regions are consistently located to the right of the pre-launch boresight vector



(Fig. 3b, e, and h) because the simulated end of the overlap needs to be delayed from the predictions assuming the pre-launch boresight vector (Fig. 2).

225 As a representative measure of the total misfit between the observation and simulations, we computed the RMS of the timing gaps at both the start and the end of the overlap (Fig. 3c, f, and i). The total misfit maps suggest a potential offset of the GALA boresight vector in the positive x direction of the spacecraft reference frame.

4.2 Direct comparison in noise magnitude and pattern

230 A discrepancy between the observed and simulated increase of the noise level assuming the pre-launch boresight vector is also evident in the absolute noise magnitude of GALA. Figure 4 presents a direct comparison between the observed GALA noise and the JANUS-based simulations during the period when the GALA FOV overlaps with the Earth. Based on Equations (1)–(6), a simulation assuming the pre-launch boresight vector predicts systematically higher noise levels, indicating an inconsistency with the pre-launch boresight assumption.

235 This inconsistency is also apparent in the temporal pattern of the GALA noise. For example, the observations exhibit local noise maxima at 09:39–09:40 and 09:42–09:43, whereas a simulation using the pre-launch boresight vector rather predicts local minima at these times. In addition, the observed noise shows a clear gradual increase after 09:47, while the simulated noise remains comparatively flat or even slightly decreases. Aside from a noise drop around 09:59, the overall temporal behavior of the observed noise supports the possible presence of a systematic offset in the GALA Rx-LoS alignment. Thus, both the absolute noise magnitude and its temporal pattern indicate the need to adjust the boresight direction.

240 The noise magnitude and temporal pattern can also be exploited for in-flight calibration of the GALA Rx-LoS alignment. Following the approach described in section 4.1, we repeated the comparison shown in Fig. 4 while varying the assumed GALA Rx-LoS. After converting the JANUS-measured radiance averaged within the GALA FOV into GALA noise levels (see Sect. 3), discrepancies between the observation and simulations were evaluated in two ways. First, the mean difference between the observed and simulated noise levels was computed as a measure of agreement in absolute noise magnitude. Second, the correlation coefficient of the temporal noise variations was calculated to quantify how well the simulations reproduce the 245 observed temporal variability. In both analyses, we use only data acquired during the period of increased noise, namely the duration between the first and last Juice attitude acquisitions while the elevated noise level was observed (indicated by the two vertical extended gray lines in Fig. 4).

250 Two approaches were adopted regarding the temporal resolution of the comparison. In the first approach, all observations were compared with simulations based on interpolated Juice attitude information. This approach provides higher temporal resolution but introduces uncertainty associated with attitude interpolation between discrete measurements. Note that we present results obtained with the linear interpolation hereafter, because only negligible differences were found among the three interpolation methods. In the second approach, only data points corresponding to the actual Juice attitude acquisition times were used. Although this approach reduces the number of used data points, it eliminates uncertainties introduced by interpolations. While the final results obtained using these two approaches are broadly consistent, the differences are not entirely negligible.



255 Optimization of the GALA Rx-LoS alignment based on noise magnitude reveals two candidate regions of boresight vectors
that yield simulations consistent with the observations. In Fig. 5a and b, two irregular ring-shaped regions indicate where the
mean simulated noise magnitude matches the observed values well. Both regions partially overlap with the region where the
total RMS residual of the start and end times of the noise increase is less than 15 seconds. This overlap suggests that the
true GALA Rx-LoS may lie within either of these two areas. In contrast, the simulation using the pre-launch boresight vector
260 predicts noise magnitude levels approximately 0.1 mV higher than the observation, as depicted in Fig. 4.

The temporal correlation of the noise pattern also provides additional constraints on the GALA boresight vector. Figure
5c and d show the distributions of correlation coefficients for different boresight directions. In both temporal-resolution ap-
proaches, the pre-launch boresight vector yields a negative correlation coefficient, reflecting discrepancies in temporal features
265 such as the initial noise maximum (Fig. 4). The highest correlation coefficients are instead obtained for boresight vectors
shifted by approximately $700 \mu\text{rad}$ from the pre-launch direction (white triangles in Fig. 5). Although the precise locations of
maximum correlation differ slightly between the two temporal-resolution methods, the overall distributions are qualitatively
similar.

270 By combining constraints from the start and end timings of the noise increase, the absolute noise magnitude, and the tem-
poral noise pattern, the most likely boresight solution is found at distinct locations from the pre-launch measurement. Among
boresight vectors for which the RMS of the timing residuals is less than 15 seconds and the absolute mean noise difference
is less than 0.25 mV, the boresight vector yielding the maximum temporal correlation is selected as representative for each
275 temporal-resolution approach (white stars in Fig. 5). In the spacecraft reference frame, the most-likely boresight directions are
defined as $(-315 \mu\text{rad}, 500 \mu\text{rad})$ and $(-585 \mu\text{rad}, 500 \mu\text{rad})$ when our analyses are performed with and without interpolations, re-
spectively. Simulations using these two most-likely boresight vectors reproduce more consistent behaviour of the GALA noise
280 level than a simulation using the pre-launch boresight (Fig. 4). For example, the simulated noise exhibits an overall increasing
trend and reproduces the noise drop around 09:59 (UTC). Specifically in the non-interpolated case, the local maximum around
09:39–09:40 is also qualitatively captured because the GALA FOV passes a thick cloud area on the Earth (Fig. 1c). These
results imply a post-launch offset of the GALA Rx-LoS alignment relative to the pre-launch configuration by more than $700 \mu\text{rad}$, although even these most-likely solutions do not reach perfect matches with the observation, perhaps due to uncertainties
in spacecraft attitude knowledge.

5 Discussion and conclusions

Utilizing the Earth-farewell campaign of Juice as the first opportunity for in-flight calibration of GALA, we conducted a
multifaceted comparison between the observed noise floor and simulations based on JANUS image data. The results imply a
potential offset of the GALA boresight vector from its pre-launch measurement. The absolute offset from the pre-launch phase
285 may exceed $700 \mu\text{rad}$. This offset is comparable to that reported for the Lunar Orbiter Laser Altimeter (LOLA) aboard the Lunar
Reconnaissance Orbiter (LRO), where a similar magnitude of boresight variation was observed between dayside and nightside
operations due to thermal distortion (Barker et al., 2018). However, in the case of GALA, such a thermal distortion effect is



expected to be smaller based on pre-launch characterization of the instrument. Thermal-vacuum cycling tests conducted prior to launch showed that the boresight offset for operational temperatures between +41°C and -7°C was less than 100 μ rad
290 (Hussmann et al., 2025). In addition, the offset induced by launch vibrations was expected to be smaller than 700 μ rad by an order of magnitude. Therefore, no definitive physical cause for the inferred offset can be identified at present. Nevertheless, any post-launch changes in alignment can only be assessed through in-flight calibration activities such as those presented in this study. Further calibration campaigns can also be used to infer whether a potential bias in the Juice attitude knowledge could cause the observed large discrepancies with the pre-launch measurements.

295 In addition to inferring the boresight alignment, our analysis also provides a radiometric calibration of the GALA receiver, deriving an empirical relationship between the photon flux incident on the GALA APD and noise RMS. Based on Equations (5) and (6), this relationship can be expressed by fitting the observed noise RMS, N_{obs} , to the photon flux estimated from the JANUS image, P_G , using

$$N_{\text{obs}} = \sqrt{N_{\text{bg}}^2 + \alpha P_G}, \quad (8)$$

300 where N_{bg} is the background noise level of 1.12 mV, and α is a conversion coefficient determined by the fitting. Note that P_G is dependent on the assumed boresight vector in the calculation; therefore, different boresight assumptions lead to slightly different calibration lines. Figure 6 shows calibration lines obtained using various assumed GALA Rx-LoS alignments. Although the fitted calibration lines are broadly similar, the calibration line derived under the pre-launch boresight assumption yields a GALA noise RMS lower than the theoretical prediction at a given photon flux. This behavior is consistent with the 305 systematically higher simulated noise levels obtained using the pre-launch boresight vector (Fig. 4).

The calibration lines in Fig. 6 suggest that future observations will provide additional opportunities to validate and refine the GALA FOV boresight alignment using the methodology developed in this study. For example, based on the lunar radiance measured by JANUS during the Earth-farewell campaign (Fig. 1c), the GALA noise level is expected to increase by more than 110 % (black vertical line in Fig. 6). Given that the phase angle of the Moon was 70 degrees during this observation, the 310 photon flux incident on the GALA APD could increase significantly when the Moon is observed with a lower phase angle. Moreover, observations of the lunar nearside are expected to yield lower noise levels, as the JANUS image acquired during the Earth-farewell campaign captures the lunar farside with a sub-Juice longitude of 175°E. On the nearside, observations of lunar maria, which have albedo at 1064 nm approximately half that of the highlands (e.g., Lucey et al., 2014), may decrease the noise level significantly. Compared to the Earth measurement, lunar observations are less influenced by the time-varying 315 atmosphere and are more straightforward to interpret the GALA noise variation. Therefore, observation opportunities of the Moon around future Earth Gravity Assists of Juice may help further investigation of the GALA Rx-LoS alignment.

Future observations of Jupiter and Galilean moons reflectance may be also performed by GALA. Using the PSG (Villanueva et al., 2018) together with spectral catalogs of Galilean moons from Clark et al. (2007) and Jupiter from Madden and Kaltenegger (2018), we estimate GALA noise magnitudes during the upcoming flybys in the Jupiter system (vertical dashed lines in 320 Fig. 6). To estimate the maximum possible noise increase, Lambertian reflection models with zero phase angle were assumed. During all icy moon flybys, GALA may experience noise increases of 21–66 %, which is sufficiently large for boresight char-



acterization under the cold temperature condition similar to the nominal operation at Ganymede and to measure the reflectance of the surface. However, due to harsh radiation conditions present at Jupiter a significant increase of the APD dark noise level may occur, which potentially could limit the capabilities to interpret the measurements.

325 Future calibration opportunities, especially when combined with higher-frequency of Juice attitude acquisitions, will provide more favorable conditions for alignment calibration than the Earth-farewell campaign. Although the present analysis supports a post-launch offset from the pre-launch boresight vector, the inferred alignment is not yet fully conclusive. To a certain extent, discrepancies between simulations and observations remain (Fig. 4), perhaps due to uncertainties in spacecraft attitude knowledge. Due to the low temporal resolution of the Juice attitude data during the Earth-farewell campaign, the Juice attitude 330 information between its discrete measurements needs to be interpolated, particularly for comparison in the noise increase start and end epochs, possibly introducing unknown uncertainty in the analyzes. Even when only non-interpolated data are considered, the noise magnitude comparison still supports a potential offset, but the influence of attitude sampling limitations cannot be entirely excluded. To resolve this ambiguity, acquisition of higher-frequency attitude data is essential. Since the 335 comparison of interpolation methods shows differences (Fig. 3), such high-frequency data of the Juice attitude can also mitigate estimation errors associated with interpolation. Repeated application of this calibration approach during future flybys with an increased Juice attitude sampling rate will further improve our understanding of the GALA Rx-LoS alignment. Such an increase in the acquisition frequency of Juice attitude data is also mandatory for the planned two-way laser ranging experiments with ground-based satellite laser ranging stations to gain insights into the GALA FOV direction.

340 The noise-based alignment calibration demonstrated in this study is broadly applicable for other planetary laser altimeters. For instance, the Mercury Laser Altimeter (MLA) aboard the MErcury Surface, Space Environment, GEochemistry, and Ranging (MESSENGER) spacecraft had similar passive observations to detect Earthshine to refine the pointing alignment (Neumann et al., 2005; Smith et al., 2006). The same calibration approach can be applied to the BepiColombo Laser Altimeter (BELA) 345 aboard the ESA-JAXA BepiColombo mission to Mercury (Thomas et al., 2021). Because BELA measures return pulse shapes in a similar manner as GALA to infer surface albedo and roughness (Nishiyama et al., 2022, Nishiyama et al. submitted), accurate knowledge of the laser altimeter alignment with respect to imaging instruments is crucial for interpreting BELA 350 measurements in a geologic context. This noise-based technique will provide an independent calibration approach, complementary to methods based on crossovers and topographic features (e.g., Xiao et al., 2025; Noda et al., 2021), enabling validation of the boresight vector from multiple perspectives. Therefore, the methodology demonstrated in this study not only supports future GALA measurements during the Juice mission but also offers a general framework for alignment calibration of laser altimeters in planetary exploration.

Data availability. Juice cruise data are under instrument teams proprietary period until the delivery to ESA's Planetary Science Archive later during the cruise. Meanwhile, all the GALA and JANUS data presented in this study are available upon reasonable requests to HH and PP, respectively.



355 *Author contributions.* GN, AS, CH, and HH contributed to the conception and design of the study. GN, AS, KDM, CH, KaWi, KL, CA, JB, JG, KoWi, JK, KE, MK, LA, CT, LP, GP, PP, and HH contributed to data aquirement and organizing the databases. GN wrote the first draft of the paper. All authors contributed to paper revision and approved the submitted version.

Competing interests. The authors declare that they have no conflict of interest.

360 *Acknowledgements.* This work was supported by JSPS KAKENHI Grant Number JP22K21344, and JSPS Overseas Research Fellowship. Open Access funding enabled and organized by Projekt DEAL. We gratefully acknowledge the support by the JUICE project teams at ESTEC, ESOC, and ESAC. We thank the GALA Experiment teams at DLR (Institute of Space Research, Berlin), at Institute of Space and Astronautical Science (ISAS-JAXA, Tokyo), at University of Bern (Physikalisches Institut, Bern), and at Instituto de Astrofísica de Andalucía (IAA-CSIC, Granada) as well as the GALA Science Team. LA, LP, CT, and PP acknowledge support under ASI-INAF agreement n.2023-6-HH.0.



References

365 Acton, C., Bachman, N., Semenov, B., and Wright, E.: A look towards the future in the handling of space science mission geometry, *Planetary and Space Science*, 150, 9–12, <https://doi.org/10.1016/j.pss.2017.02.013>, 2018.

Akima, H.: A New Method of Interpolation and Smooth Curve Fitting Based on Local Procedures, *Journal of the ACM*, 17, 589–602, <https://doi.org/10.1145/321607.321609>, 1970.

Annex, A., Pearson, B., Seignovert, B., Carcich, B., Eichhorn, H., Mapel, J., Von Forstner, J., McAuliffe, J., Del Rio, J., Berry, K., Aye, 370 K.-M., Stefko, M., De Val-Borro, M., Kulumani, S., and Murakami, S.-y.: SpicePy: a Pythonic Wrapper for the SPICE Toolkit, *Journal of Open Source Software*, 5, 2050, <https://doi.org/10.21105/joss.02050>, 2020.

Araki, H., Tazawa, S., Noda, H., Ishihara, Y., Goossens, S., Sasaki, S., Kawano, N., Kamiya, I., Otake, H., Oberst, J., and Shum, C.: Lunar Global Shape and Polar Topography Derived from Kaguya-LALT Laser Altimetry, *Science*, 323, 897–900, <https://doi.org/10.1126/science.1164146>, 2009.

375 Barker, M. K., Sun, X., Mao, D., Mazarico, E., Neumann, G. A., Zuber, M. T., Smith, D. E., McGarry, J. F., and Hoffman, E. D.: In-flight characterization of the lunar orbiter laser altimeter instrument pointing and far-field pattern, *Applied Optics*, 57, 7702, <https://doi.org/10.1364/AO.57.007702>, 2018.

Besse, S., Yokota, Y., Boardman, J., Green, R., Haruyama, J., Isaacson, P., Mall, U., Matsunaga, T., Ohtake, M., Pieters, C., 380 Staid, M., Sunshine, J., and Yamamoto, S.: One Moon, many measurements 2: Photometric corrections, *Icarus*, 226, 127–139, <https://doi.org/10.1016/j.icarus.2013.05.009>, 2013.

Bohren, C. F. and Huffman, D. R.: *Absorption and Scattering of Light by Small Particles*, Wiley, 1 edn., ISBN 978-0-471-29340-8 978-3-527-61815-6, <https://doi.org/10.1002/9783527618156>, 1998.

Clark, R. N., Swayze, G. A., Wise, R. A., Livo, K. E., Hoefen, T. M., Kokaly, R. F., and Sutley, S. J.: USGS Digital Spectral Library splib06a, Data Series, <https://doi.org/10.3133/ds231>, series: Data Series, 2007.

385 Daly, M. G., Barnouin, O. S., Dickinson, C., Seabrook, J., Johnson, C. L., Cunningham, G., Haltigin, T., Gaudreau, D., Brunet, C., Aslam, I., Taylor, A., Bierhaus, E. B., Boynton, W., Nolan, M., and Lauretta, D. S.: The OSIRIS-REx Laser Altimeter (OLA) Investigation and Instrument, *Space Science Reviews*, 212, 899–924, <https://doi.org/10.1007/s11214-017-0375-3>, 2017.

Deutsch, A. N., Neumann, G. A., Kreslavsky, M. A., Pokorný, P., Martinez Camacho, J. M., Trang, D., Izenberg, N. R., Denevi, B. W., Galiano, A., and Filacchione, G.: Temperature-related Variations of 1064 nm Surface Reflectance on Mercury: Implications for Space 390 Weathering, *The Planetary Science Journal*, 5, 8, <https://doi.org/10.3847/PSJ/ad0e6d>, 2024.

Enya, K., Kobayashi, M., Kimura, J., Araki, H., Namiki, N., Noda, H., Kashima, S., Oshigami, S., Ishibashi, K., Yamawaki, T., Tohara, K., Saito, Y., Ozaki, M., Mizuno, T., Kamata, S., Matsumoto, K., Sasaki, S., Kuramoto, K., Sato, Y., Yokozawa, T., Numata, T., Mizumoto, S., Mizuno, H., Nagamine, K., Sawamura, A., Tanimoto, K., Imai, H., Nakagawa, H., Kirino, O., Green, D., Fujii, M., Iwamura, S., Fujishiro, N., Matsumoto, Y., Lingenauber, K., Kallenbach, R., Althaus, C., Behnke, T., Binger, J., Daurskikh, A., Eisenmenger, H., Heer, U., Hüttig, C., Lara, L. M., Lichopoj, A., Lötzke, H.-G., Lüdicke, F., Michaelis, H., Pablo Rodriguez Garcia, J., Rösner, K., Stark, A., Steinbrügge, G., Thabaut, P., Thomas, N., Del Togno, S., Wahl, D., Wendler, B., Wickhusen, K., Willner, K., and Hussmann, H.: The Ganymede Laser Altimeter (GALA) for the Jupiter Icy Moons Explorer (JUICE): Mission, science, and instrumentation of its receiver modules, *Advances in Space Research*, 69, 2283–2304, <https://doi.org/10.1016/j.asr.2021.11.036>, 2022.

Fletcher, L. N., Cavalie, T., Grassi, D., Hueso, R., Lara, L. M., Kaspi, Y., Galanti, E., Greathouse, T. K., Molyneux, P. M., Galand, M., Vallat, 400 C., Witasse, O., Lorente, R., Hartogh, P., Poulet, F., Langevin, Y., Palumbo, P., Gladstone, G. R., Rutherford, K. D., Dougherty, M. K.,



Wahlund, J.-E., Barabash, S., Iess, L., Bruzzone, L., Hussmann, H., Gurvits, L. I., Santolik, O., Kolmasova, I., Fischer, G., Müller-Wodarg, I., Piccioni, G., Fouchet, T., Gérard, J.-C., Sánchez-Lavega, A., Irwin, P. G. J., Grodent, D., Altieri, F., Mura, A., Drossart, P., Kammer, J., Giles, R., Cazaux, S., Jones, G., Smirnova, M., Lellouch, E., Medvedev, A. S., Moreno, R., Rezac, L., Coustenis, A., and Costa, M.: Jupiter Science Enabled by ESA's Jupiter Icy Moons Explorer, *Space Science Reviews*, 219, 53, <https://doi.org/10.1007/s11214-023-00996-6>, 2023.

405 Fritsch, F. N. and Butland, J.: A Method for Constructing Local Monotone Piecewise Cubic Interpolants, *SIAM Journal on Scientific and Statistical Computing*, 5, 300–304, <https://doi.org/10.1137/0905021>, 1984.

Hussmann, H., Lingenauber, K., Kallenbach, R., Enya, K., Thomas, N., Lara, L. M., Althaus, C., Araki, H., Behnke, T., Castro-Marin, J. M., Eisenmenger, H., Gerber, T., Herranz De La Revilla, M., Hüttig, C., Ishibashi, K., Jiménez-Ortega, J., Kimura, J., Kobayashi, M., Lötzke, H.-G., Lichopoj, A., Lüdicke, F., Martínez-Navajas, I., Michaelis, H., Namiki, N., Noda, H., Oberst, J., Oshigami, S., Rodríguez García, J. P., Rodrigo, J., Rösner, K., Stark, A., Steinbrügge, G., Thabaut, P., Del Togno, S., Touhara, K., Villamil, S., Wendler, B., Wickhusen, K., and Willner, K.: The Ganymede laser altimeter (GALA): key objectives, instrument design, and performance, *CEAS Space Journal*, 11, 381–390, <https://doi.org/10.1007/s12567-019-00282-8>, 2019.

410 Hussmann, H., Lingenauber, K., Stark, A., Enya, K., Thomas, N., Lara, L. M., Althaus, C., Araki, H., Behnke, T., Binger, J., Breuer, D., Casotto, S., Castro, J. M., Choblet, G., Christensen, U., Coppolse, W., Eisenmenger, H., Ferraz-Mello, S., Fujii, M., Fujishiro, N., Gallina, G., Gwinner, K., Hauber, E., Heer, U., Henkelmann, R., Herranz, M., Hüttig, C., Iwamura, S., Jiménez, J., Kimura, J., Kirino, O., Kobayashi, M., Kurita, K., Lainey, V., Leikert, T., Lichopoj, A., Lötzke, H.-G., Lüdicke, F., Martínez-Navajas, I., Michaelis, H., Nakagawa, H., Namiki, N., Nishiyama, G., Noda, H., Oberst, J., Oshigami, S., Pommerol, A., Rech, M., Roatsch, T., Rodrigo, R., Rodríguez, A., Rösner, K., Touhara, K., Saito, Y., Sasaki, S., Sato, Y., Schmidt, F., Schreiber, U., Schulze-Walewski, S., Sohl, F., Spohn, T., Steinbrügge, G., Stephan, K., Tanimoto, K., Thabaut, P., Del Togno, S., Vermeersen, B., Wegert, H., Weidlich, K., Wendler, B., Wickhusen, K., Wieczorek, M., Willner, K., Wolff, F., Yokozawa, T., and Yseboodt, M.: The Ganymede Laser Altimeter (GALA) on the Jupiter Icy moons Explorer (JUICE) Mission, *Space Science Reviews*, 221, 33, <https://doi.org/10.1007/s11214-025-01149-7>, 2025.

420 Kamata, S., Kimura, J., Matsumoto, K., Nimmo, F., Kuramoto, K., and Namiki, N.: Tidal deformation of Ganymede: Sensitivity of Love numbers on the interior structure, *Journal of Geophysical Research: Planets*, 121, 1362–1375, <https://doi.org/10.1002/2016JE005071>, 2016.

425 Kikuchi, S., Saiki, T., Takei, Y., Terui, F., Ogawa, N., Mimasu, Y., Ono, G., Yoshikawa, K., Sawada, H., Takeuchi, H., Ikeda, H., Fujii, A., Sugita, S., Morota, T., Yamada, M., Honda, R., Yokota, Y., Sakatani, N., Kameda, S., Kouyama, T., Hirata, N., Hirata, N., Shirai, K., Kitazato, K., Nakazawa, S., Yoshikawa, M., Tanaka, S., Wada, K., Watanabe, S.-i., and Tsuda, Y.: Hayabusa2 pinpoint touchdown near the artificial crater on Ryugu: Trajectory design and guidance performance, *Advances in Space Research*, 68, 3093–3140, <https://doi.org/10.1016/j.asr.2021.07.031>, 2021.

430 Kimura, J., Hussmann, H., Kamata, S., Matsumoto, K., Oberst, J., Steinbrügge, G., Stark, A., Gwinner, K., Oshigami, S., Namiki, N., Lingenauber, K., Enya, K., Kuramoto, K., and Sasaki, S.: Science Objectives of the Ganymede Laser Altimeter (GALA) for the JUICE Mission, *TRANSACTIONS OF THE JAPAN SOCIETY FOR AERONAUTICAL AND SPACE SCIENCES, AEROSPACE TECHNOLOGY JAPAN*, 17, 234–243, <https://doi.org/10.2322/tastj.17.234>, 2019.

435 Lucey, P. G., Neumann, G. A., Riner, M. A., Mazarico, E., Smith, D. E., Zuber, M. T., Paige, D. A., Bussey, D. B., Cahill, J. T., McGovern, A., Isaacson, P., Corley, L. M., Torrence, M. H., Melosh, H. J., Head, J. W., and Song, E.: The global albedo of the Moon at 1064 nm from LOLA: THE GLOBAL ALBEDO OF THE MOON FROM LOLA, *Journal of Geophysical Research: Planets*, 119, 1665–1679, <https://doi.org/10.1002/2013JE004592>, 2014.



440 Madden, J. and Kaltenegger, L.: A Catalog of Spectra, Albedos, and Colors of Solar System Bodies for Exoplanet Comparison, *Astrobiology*, 18, 1559–1573, <https://doi.org/10.1089/ast.2017.1763>, 2018.

Mizuno, T., Kase, T., Shiina, T., Mita, M., Namiki, N., Senshu, H., Yamada, R., Noda, H., Kunimori, H., Hirata, N., Terui, F., and Mimasu, Y.: Development of the Laser Altimeter (LIDAR) for Hayabusa2, *Space Science Reviews*, 208, 33–47, <https://doi.org/10.1007/s11214-015-0231-2>, 2017.

445 Neumann, G. A., Abshire, J. B., Aharonson, O., Garvin, J. B., Sun, X., and Zuber, M. T.: Mars Orbiter Laser Altimeter pulse width measurements and footprint-scale roughness, *Geophysical Research Letters*, 30, 2003GL017048, <https://doi.org/10.1029/2003GL017048>, 2003.

Neumann, G. A., Smith, D. E., Zuber, M. T., Sun, X., Cavanaugh, J. F., McGarry, J. F., and Zagwodski, T. W.: An asynchronous laser transponder experiment in deep space using MESSENGER’s Mercury Laser Altimeter, vol. 2005, pp. G51A–0808, <https://ui.adsabs.harvard.edu/abs/2005AGUFM.G51A0808N>, 2005.

450 Nishiyama, G., Stark, A., Hüttig, C., Hussmann, H., Gwinner, K., Hauber, E., M. Lara, L., and Thomas, N.: Simulation of laser pulse shapes received by the BepiColombo Laser Altimeter (BELA): Implications for future constraints on surficial properties of Mercury, <https://doi.org/10.5194/epsc2022-326>, 2022.

Nishiyama, G., Suzuki, Y., Uno, S., Aoki, S., Iwanaka, T., Imamura, T., Fujii, Y., Müller, T. G., Taguchi, M., Kouyama, T., Barraud, O., D’Amore, M., Helbert, J., and Adeli, S.: Temporal variation in the cloud-top temperature of Venus revealed by meteorological satellites, <https://doi.org/10.21203/rs.3.rs-5884016/v1>, 2025.

455 Noda, H., Kunimori, H., Mizuno, T., Senshu, H., Ogawa, N., Takeuchi, H., Moore, C., Pollard, A., Yamaguchi, T., Namiki, N., Kase, T., Saiki, T., and Tsuda, Y.: Laser link experiment with the Hayabusa2 laser altimeter for in-flight alignment measurement, *Earth, Planets and Space*, 69, 2, <https://doi.org/10.1186/s40623-016-0589-8>, 2017.

Noda, H., Senshu, H., Matsumoto, K., Namiki, N., Mizuno, T., Sugita, S., Abe, S., Araki, H., Asari, K., Cho, Y., Fujii, A., Hayakawa, M., Higuchi, A., Hirata, N., Hirata, N., Honda, C., Honda, R., Ishihara, Y., Kameda, S., Kikuchi, S., Kouyama, T., Matsuoka, M., Mimasu, Y., 460 Morota, T., Nakazawa, S., Ogawa, K., Ogawa, N., Ono, G., Oshigami, S., Saiki, T., Sakatani, N., Sasaki, S., Sawada, H., Shizugami, M., Suzuki, H., Takahashi, T., Takei, Y., Tanaka, S., Tatsumi, E., Terui, F., Tsuda, Y., Tsuruta, S., Watanabe, S.-i., Yamada, M., Yamada, R., Yamaguchi, T., Yamamoto, K., Yokota, Y., Yoshida, F., Yoshikawa, K., Yoshikawa, M., and Yoshioka, K.: Alignment determination of the Hayabusa2 laser altimeter (LIDAR), *Earth, Planets and Space*, 73, 21, <https://doi.org/10.1186/s40623-020-01342-8>, 2021.

Noda, H., Senshu, H., Otsubo, T., Takeuchi, H., Courde, C., Kunimori, H., Moore, C., Schreiber, U., Ogawa, N., Saiki, T., Takei, Y., Aimar, 465 M., Chabé, J., Eckl, J., Kamata, S., Higuchi, A., Hirai, T., Martinot-Lagarde, G., Mariey, H., Matsumoto, K., Maurice, N., Nakazono, J., Phung, D.-H., Scariot, J., Suetsugu, R., Torre, J.-M., Pollard, A., Viot, H., Namiki, N., and Mizuno, T.: Demonstration of deep-space synchronous two-way laser ranging with a laser transponder aboard Hayabusa2, *Advances in Space Research*, 71, 4196–4209, <https://doi.org/10.1016/j.asr.2022.12.057>, 2023.

Ohtake, M., Pieters, C., Isaacson, P., Besse, S., Yokota, Y., Matsunaga, T., Boardman, J., Yamamoto, S., Haruyama, J., Staid, M., Mall, U., and 470 Green, R.: One Moon, Many Measurements 3: Spectral reflectance, *Icarus*, 226, 364–374, <https://doi.org/10.1016/j.icarus.2013.05.010>, 2013.

Okuyama, A., Takahashi, M., Date, K., Hosaka, K., Murata, H., Tabata, T., and Yoshino, R.: Validation of Himawari-8/AHI Radiometric Calibration Based on Two Years of In-Orbit Data, *Journal of the Meteorological Society of Japan. Ser. II*, 96B, 91–109, <https://doi.org/10.2151/jmsj.2018-033>, 2018.

475 Palumbo, P., Roatsch, T., Lara, L. M., Castro-Marin, J. M., Della Corte, V., Hviid, S., Jaumann, R., Michaelis, H., Patel, M. R., Portyankina, G., Schmitz, N., Amoroso, M., Mugnuolo, R., Aboudan, A., Agostini, L., Althaus, C., Álvarez, F., Bartolomei, M., Behnke, T., Bilotta,



T., Colombatti, G., Colosimo, A., Coustenis, A., Cremonese, G., Crews, C., Dattolo, A., Debei, S., Denk, T., Fiethe, B., Herranz, M., Hoffmann, H., Hueso, R., Koncz, A., Jiménez-Ortega, J., Lichopoj, A., Livi, L., Llamas, X., Lopes, R., Lucchetti, A., Martinez-Navajas, I., Mazzotta Epifani, E., Mertens, V., Pajola, M., Sarti, F., Schroedter, R., Stephan, K., Tosi, F., Tubiana, C., Wendler, B., Wendler, D., Williams, D., Wolff, F., Zusi, M., Chiodini, S., Ficai Veltroni, I., Galeotti, A., García-Segura, A., Greggio, D., Holland, A. D., Kenkmann, T., Leese, M. R., Magrin, D., Michalik, H., Munari, M., Noci, G. E., Paolinetti, R., Schipani, P., Soman, M., Stefanov, K. D., Turella, A., Aharonson, O., Bell, J. F., Bertini, I., Coates, A. J., Di Achille, G., Grassi, D., Groussin, O., Gwinner, K., Haruyama, J., Hauber, E., Hiesinger, H., Langevin, Y., Lainey, V., Marchi, S., Marinangeli, L., Marzari, F., Massironi, M., Mitri, G., Mottola, S., Oberst, J., Postberg, F., Poulet, F., Preusker, F., Schmidt, J., Schneider, N. M., Simon, A., Takahashi, Y., Tirsch, D., Vincendon, M., Balme, M. R., Bettanini, C., Borin, P., Capria, M. T., Elgner, S., Esposito, F., Ferranti, L., Ferrari, S., Fornasier, S., Galluzzi, V., Giacomini, L., Guzzetta, L., Jones, G. H., Kersten, E., Ledeit, L., Martellato, E., Matz, K.-D., Mennella, V., Murray, C., Otto, K. A., Pelizzo, M. G., Penasa, L., Politi, R., Popa, C., Pozzobon, R., Prieto Ballesteros, O., Re, C., Rotundi, A., Sato, M., Schmedemann, N., Shoji, D., Simioni, E., Sindoni, G., Trauthan, F., and Yair, Y.: The JANUS (Jovis Amorum ac Natorum Undique Scrutator) VIS-NIR Multi-Band Imager for the JUICE Mission, *Space Science Reviews*, 221, 32, <https://doi.org/10.1007/s11214-025-01158-6>, 2025.

480 490 Pieters, C., Boardman, J., Ohtake, M., Matsunaga, T., Haruyama, J., Green, R., Mall, U., Staid, M., Isaacson, P., Yokota, Y., Yamamoto, S., Besse, S., and Sunshine, J.: One Moon, many measurements 1: Radiance values, *Icarus*, 226, 951–963, <https://doi.org/10.1016/j.icarus.2013.07.008>, 2013.

Smith, D. E., Zuber, M. T., Sun, X., Neumann, G. A., Cavanaugh, J. F., McGarry, J. F., and Zagwodzki, T. W.: Two-Way Laser Link over Interplanetary Distance, *Science*, 311, 53–53, <https://doi.org/10.1126/science.1120091>, 2006.

495 500 Smith, D. E., Zuber, M. T., Neumann, G. A., Mazarico, E., Lemoine, F. G., Head III, J. W., Lucey, P. G., Aharonson, O., Robinson, M. S., Sun, X., Torrence, M. H., Barker, M. K., Oberst, J., Duxbury, T. C., Mao, D., Barnouin, O. S., Jha, K., Rowlands, D. D., Goossens, S., Baker, D., Bauer, S., Gläser, P., Lemelin, M., Rosenburg, M., Sori, M. M., Whitten, J., and Mcclanahan, T.: Summary of the results from the lunar orbiter laser altimeter after seven years in lunar orbit, *Icarus*, 283, 70–91, <https://doi.org/10.1016/j.icarus.2016.06.006>, 2017.

Stark, A., Oberst, J., Preusker, F., Gwinner, K., Peale, S. J., Margot, J.-L., Phillips, R. J., Zuber, M. T., and Solomon, S. C.: Mercury's rotational parameters from MESSENGER image and laser altimeter data: A feasibility study, *Planetary and Space Science*, 117, 64–72, <https://doi.org/10.1016/j.pss.2015.05.006>, 2015a.

Stark, A., Oberst, J., Preusker, F., Peale, S. J., Margot, J., Phillips, R. J., Neumann, G. A., Smith, D. E., Zuber, M. T., and Solomon, S. C.: First MESSENGER orbital observations of Mercury's librations, *Geophysical Research Letters*, 42, 7881–7889, <https://doi.org/10.1002/2015GL065152>, 2015b.

505 Stark, A., Hussmann, H., Althaus, C., Behnke, T., Binger, J., Choblet, G., Enya, K., Ferraz Mello, S., George, J. P., Hüttig, C., Kimura, J., Lingenauber, K., Nishiyama, G., Oberst, J., Palumbo, P., Portyankina, G., Tubiana, C., Wickhusen, K., Willner, K., Wieczorek, M., and GALA team: Performance of the Ganymede Laser Altimeter (GALA) based on cruise measurements, <https://doi.org/10.5194/epsc2024-871>, 2024.

Steinbrügge, G., Stark, A., Hussmann, H., Wickhusen, K., and Oberst, J.: The performance of the BepiColombo Laser Altimeter (BELA) prior launch and prospects for Mercury orbit operations, *Planetary and Space Science*, 159, 84–92, <https://doi.org/10.1016/j.pss.2018.04.017>, 2018.

Thomas, N., Hussmann, H., Spohn, T., Lara, L. M., Christensen, U., Affolter, M., Bandy, T., Beck, T., Chakraborty, S., Geissbuehler, U., Gerber, M., Ghose, K., Gouman, J., HosseiniArani, S., Kuske, K., Peteut, A., Piazza, D., Rieder, M., Servonet, A., Althaus, C., Behnke, T., Gwinner, K., Hüttig, C., Kallenbach, R., Lichopoj, A., Lingenauber, K., Lötzke, H.-G., Lüdicke, F., Michaelis, H., Oberst, J., Schrödter,



515 R., Stark, A., Steinbrügge, G., Del Togno, S., Wickhusen, K., Castro, J. M., Herranz, M., Rodrigo, J., Perplies, H., Weigel, T., Schulze-
Walewski, S., Blum, S., Casciello, A., Rugi-Grond, E., Coppolose, W., Rech, M., Weidlich, K., Leikert, T., Henkelmann, R., Trefzger, B.,
and Metz, B.: The BepiColombo Laser Altimeter, *Space Science Reviews*, 217, 25, <https://doi.org/10.1007/s11214-021-00794-y>, 2021.

520 Tosi, F., Roatsch, T., Galli, A., Hauber, E., Lucchetti, A., Molyneux, P., Stephan, K., Achilleos, N., Bovolo, F., Carter, J., Cavalie, T., Cimò,
G., D'Aversa, E., Gwinner, K., Hartogh, P., Huybrighs, H., Langevin, Y., Lellouch, E., Migliorini, A., Palumbo, P., Piccioni, G., Plaut, J. J.,
Postberg, F., Poulet, F., Retherford, K., Rezac, L., Roth, L., Solomonidou, A., Tobie, G., Tortora, P., Tubiana, C., Wagner, R., Wirström,
E., Wurz, P., Zambon, F., Zannoni, M., Barabash, S., Bruzzone, L., Dougherty, M., Gladstone, R., Gurvits, L. I., Hussmann, H., Iess, L.,
Wahlund, J.-E., Witasse, O., Vallat, C., and Lorente, R.: Characterization of the Surfaces and Near-Surface Atmospheres of Ganymede,
Europa and Callisto by JUICE, *Space Science Reviews*, 220, 59, <https://doi.org/10.1007/s11214-024-01089-8>, 2024.

525 Villanueva, G., Smith, M., Protopapa, S., Faggi, S., and Mandell, A.: Planetary Spectrum Generator: An accurate online radiative transfer
suite for atmospheres, comets, small bodies and exoplanets, *Journal of Quantitative Spectroscopy and Radiative Transfer*, 217, 86–104,
<https://doi.org/10.1016/j.jqsrt.2018.05.023>, 2018.

Xiao, H., Stark, A., Steinbrügge, G., Briaud, A., Lara, L. M., and Gutiérrez, P. J.: Mercury's Tidal Love Number h_2 From
Co-Registration of MLA Profiles, *Geophysical Research Letters*, 52, e2024GL112266, <https://doi.org/10.1029/2024GL112266>, 2025.

530 Yumoto, K., Tatsumi, E., Kouyama, T., Golish, D., Cho, Y., Morota, T., Kameda, S., Sato, H., Rizk, B., DellaGiustina, D., Yokota, Y.,
Suzuki, H., De León, J., Campins, H., Licandro, J., Popescu, M., Rizos, J., Honda, R., Yamada, M., Sakatani, N., Honda, C., Mat-
suoka, M., Hayakawa, M., Sawada, H., Ogawa, K., Yamamoto, Y., Lauretta, D., and Sugita, S.: Comparison of optical spectra be-
tween asteroids Ryugu and Bennu: I. Cross calibration between Hayabusa2/ONC-T and OSIRIS-REx/MapCam, *Icarus*, 417, 116122,
<https://doi.org/10.1016/j.icarus.2024.116122>, 2024.

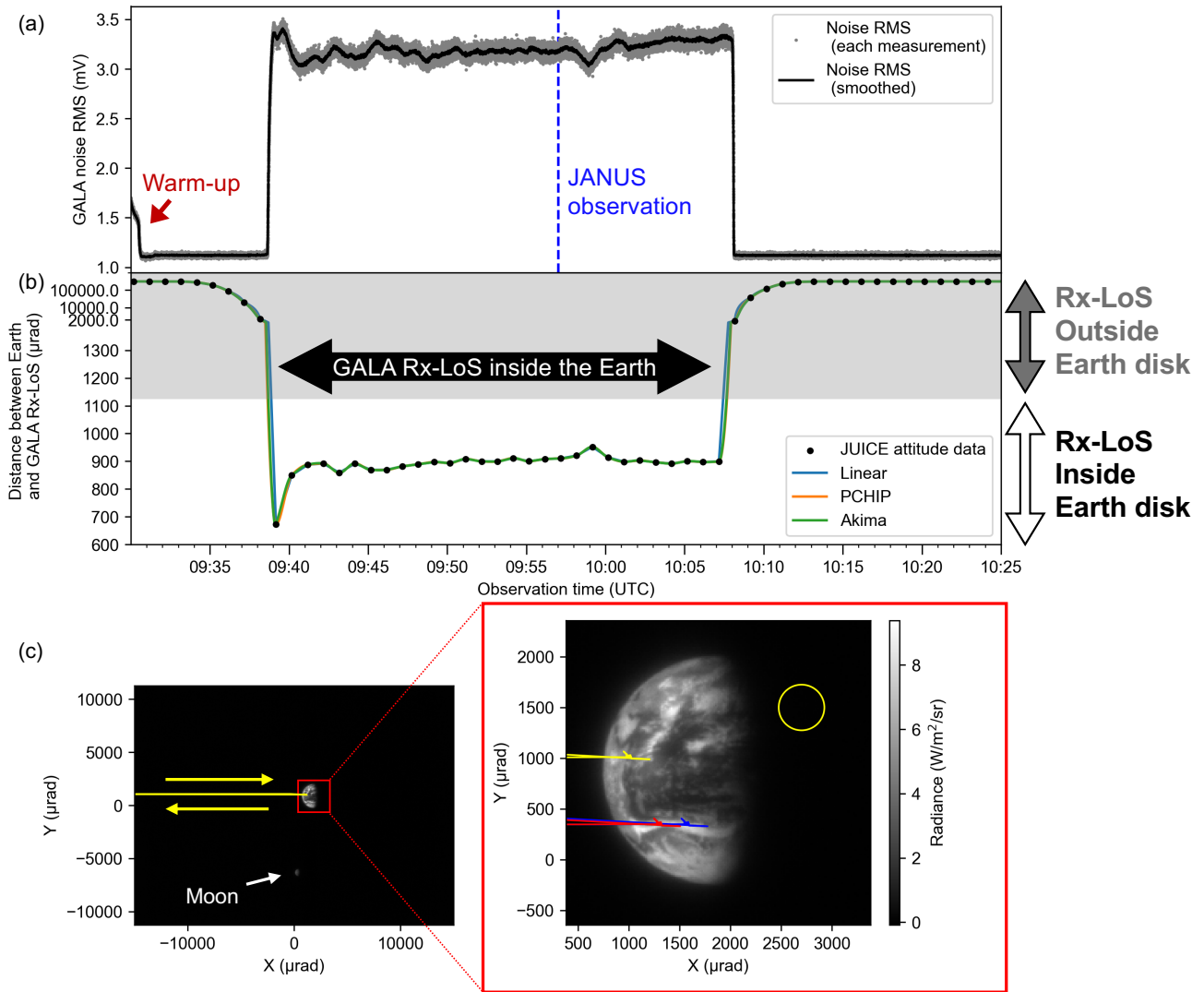


Figure 1. Data used in this study. (a) GALA noise data acquired during the Earth-farewell campaign. The blue dashed line indicates the time at which the JANUS image used in this study was obtained. (b) Angular distance between the Earth center and the GALA Rx-LoS. The gray shaded region indicates the angular distance when the Rx-LoS is outside the Earth. The black points denote the acquisition times of the Juice attitude data (separated by one minute). The colored lines show angular distances interpolated with different methods. Note that y-axis values above and below 1400 μ rad are shown on logarithmic and linear scales, respectively. (c) JANUS images taken on 2024/09/09 at 09:57:02 (UTC). The full frame and and zoomed-in images are shown in the left and right panels, respectively. The yellow line indicates the location of the GALA Rx-LoS assuming the GALA-base direction measured in the pre-launch phase. The yellow circle denotes the size of the GALA FOV on the JANUS image for reference. The red and blue lines in the right panel show GALA Rx-LoS locations calculated with most-likely boresight vectors derived using all interpolated attitude data and using only the discrete Juice attitude acquisition times, respectively (see details in Sect. 4).

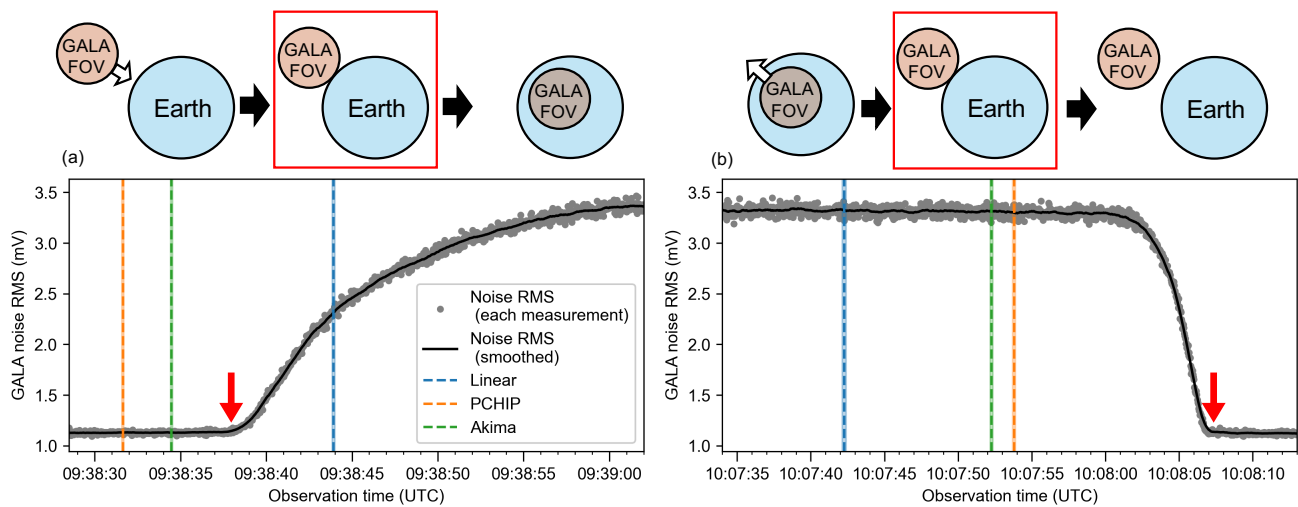


Figure 2. GALA noise data around the start and end of the noise increase with schematic illustrations. (a) Noise RMS around the start of the noise increase. The upper panel shows a schematic view of the GALA FOV position relative to the Earth. The onset of the noise increase, indicated by the red arrow, corresponds to the configuration of the red-boxed schematic illustration. The colored vertical dashed lines indicate the simulated start of the overlap using different interpolation methods. The colored vertical bands show possible timing uncertainties in the simulations due to the effect of the Earth's atmosphere. (b) Noise RMS around the end of the overlap, plotted in the same manner as (a).

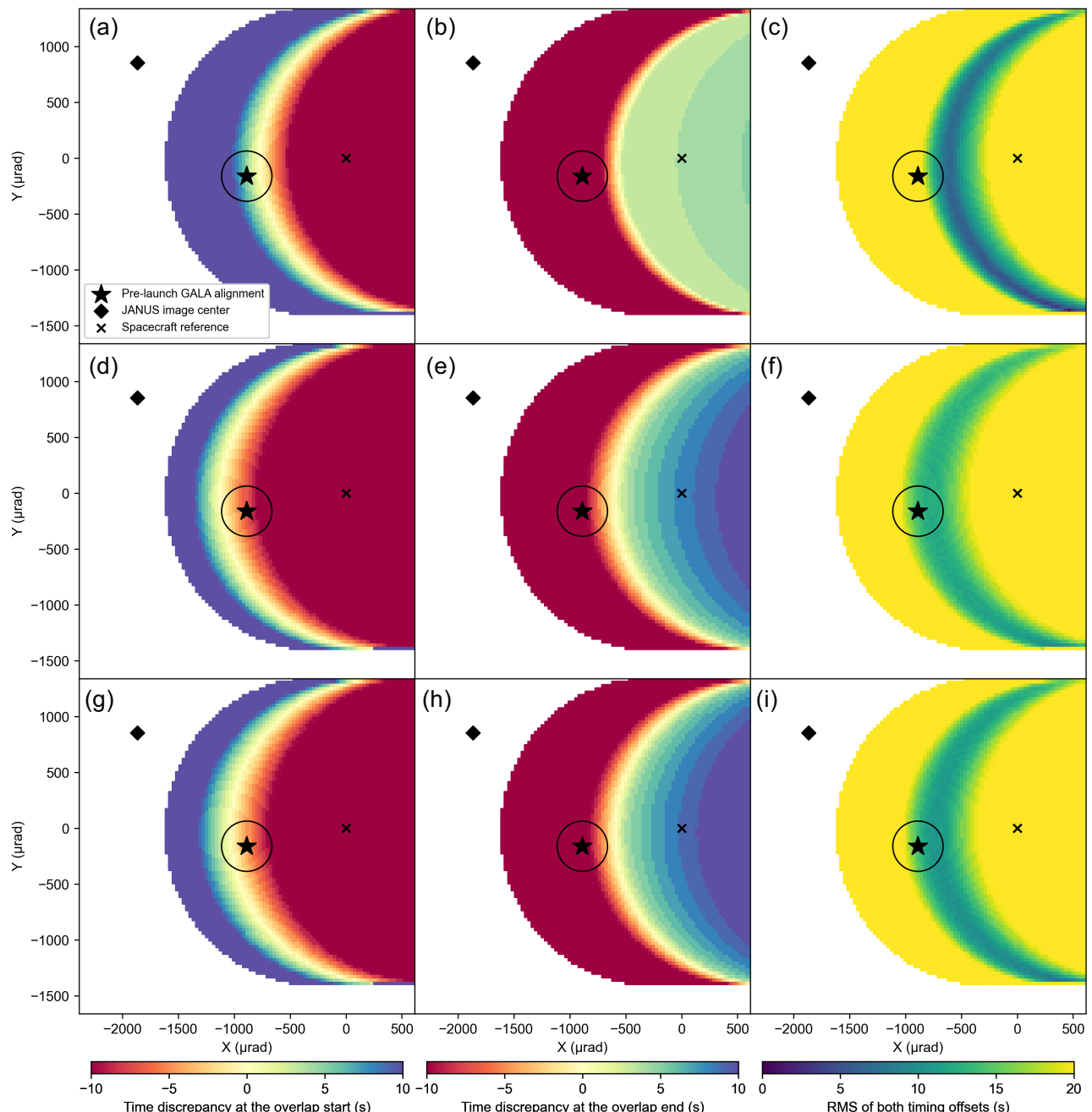


Figure 3. Optimization results of the overlap start and end. (a, d, g) Maps of the time discrepancies between the simulated and observed start of the noise increase as a function of the assumed GALA boresight direction. The color map indicates the time differences obtained by subtracting the observed start time from the simulated start time. The white regions indicate parameter areas where the GALA FOV never intersects with the Earth. (b, e, h) Same maps for the end of noise increase. (c, f, i) Maps of total time residual for both the start and end of the noise increase. In all panels, the black star, diamond, and cross marks denote the pre-launch GALA boresight, the center of JANUS image frame, and the spacecraft reference, respectively. The dark circle indicates the size of the GALA FOV. Results obtained using the linear, PCHIP, and Akima interpolations are shown in (a, b, c), (d, e, f), and (g, h, i), respectively. Note that each boresight vector is defined as $(x, y, \sqrt{1 - x^2 - y^2})$ in the spacecraft reference frame, where x and y are the coordinates shown in the plots.

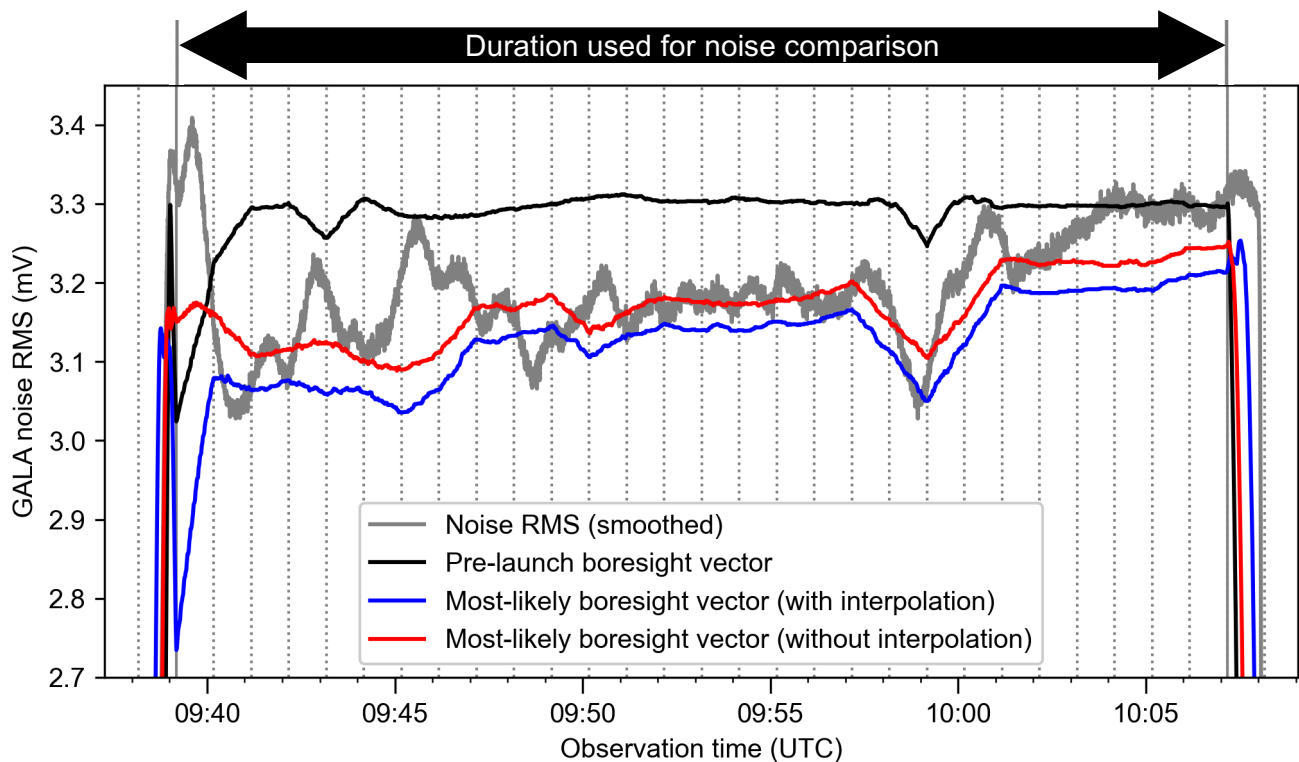


Figure 4. Comparison of the magnitude and temporal pattern of the increased noise between the observation and simulations. The vertical gray dotted lines indicate acquisition times of the Juice attitude data. For direct comparison between observed and simulated GALA noise, only the duration between the two vertical gray solid lines is used. The linear interpolation is applied to the simulations shown in this plot.

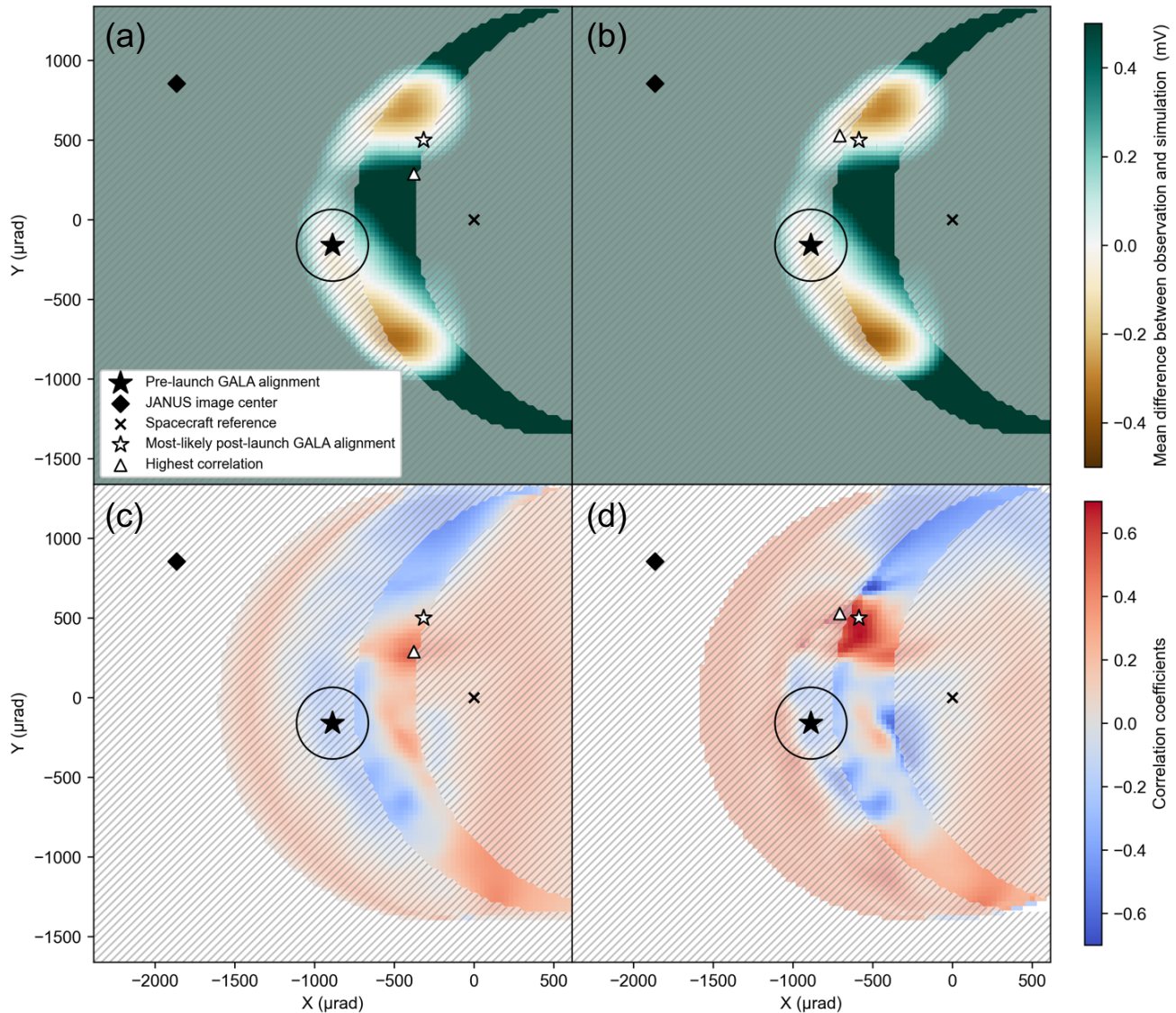


Figure 5. Optimization results of the GALA Rx-LoS alignment based on the noise magnitude and temporal pattern. (a, b) Optimization based on the increased noise magnitude. The color scale indicates the mean difference obtained by subtracting the simulated noise from the observed noise. (c, d) Optimization based on the temporal variation of the noise. The white triangles denote the boresight vector with the highest correlation coefficients. Results obtained using all interpolated attitude points and using only the discrete Juice attitude acquisition times are shown in panels (a, c) and (b, d), respectively. Note that the linear interpolation is used for the simulations in this plot. In all panels, the white stars indicate the locations of the most-likely boresight vectors shown as the red and blue lines in Fig. 4. The boresight vectors for which the RMS residual of the start and end timings exceeds 15 seconds are shaded in white.

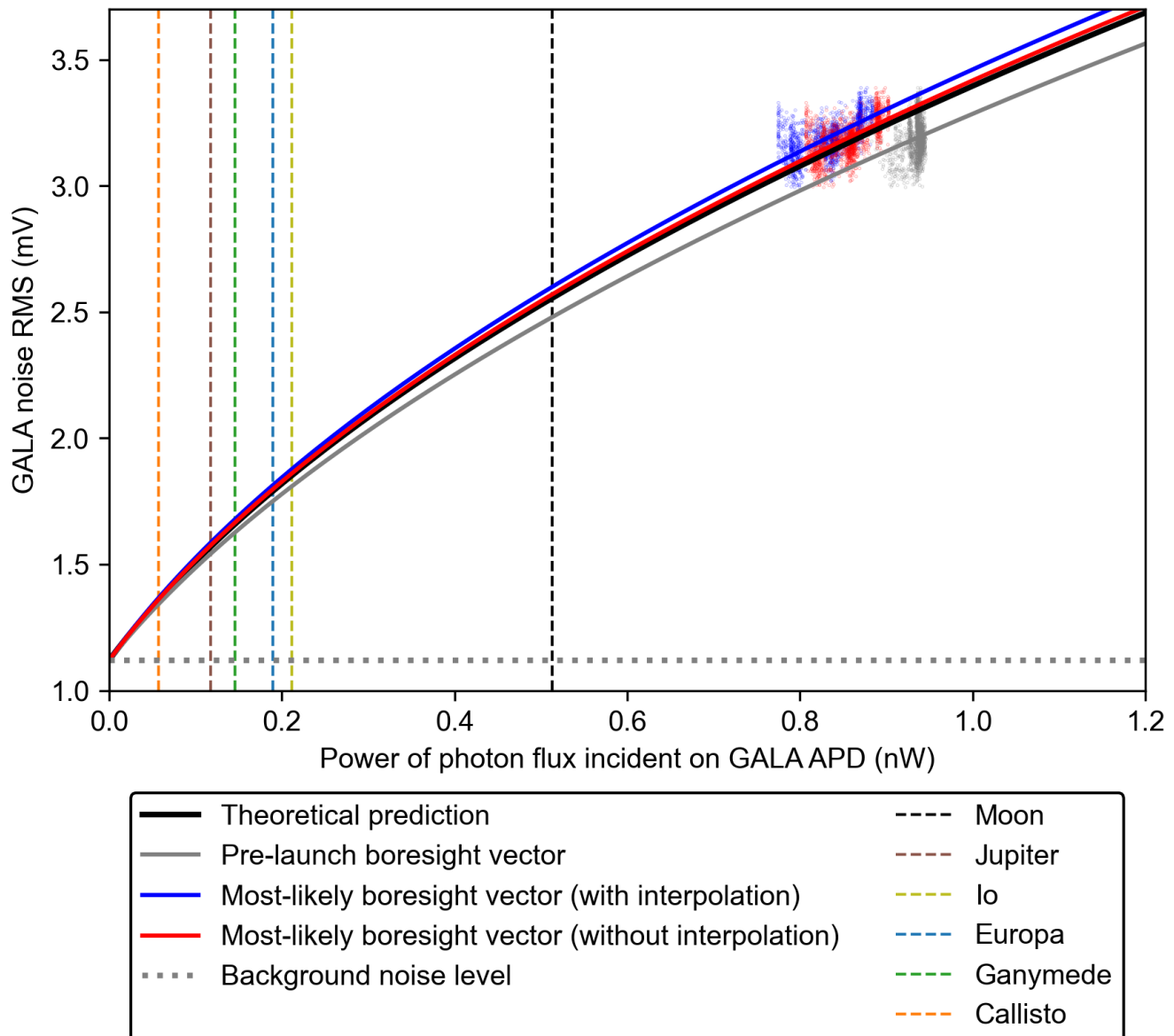


Figure 6. Calibration lines between the power of photon flux incident on the GALA APD and the GALA noise RMS. The colored points are values used to fit Equation (8).